

# 4D Wavelet-Based Regularization for Parallel MRI Reconstruction: Impact on Subject and Group-Levels Statistical Sensitivity in fMRI

Lotfi Chaari<sup>1,2</sup>, Sébastien Mériaux<sup>2</sup>, Solveig Badillo<sup>2</sup>, Jean-Christophe Pesquet<sup>3</sup> and Philippe Ciuciu<sup>2</sup>

<sup>1</sup> *INRIA Rhône-Alpes, 655 avenue de l'Europe, Montbonnot  
38334 Saint Ismier Cedex, France: lotfi.chaari@inria.fr*

<sup>2</sup> *CEA/DSV/I<sup>2</sup>BM/Neurospin, CEA Saclay, Bbt. 145, Point  
Courrier 156, 91191 Gif-sur-Yvette cedex, France:  
{sebastien.meriaux,philippe.ciuciu}@cea.fr*

<sup>3</sup> *Université Paris-Est, IGM and UMR-CNRS 8049, 77454  
Marne-la-Vallée cedex, France:  
jean-christophe.pesquet@univ-paris-est.fr*

---

## Abstract

Parallel MRI is a fast imaging technique that enables the acquisition of highly resolved images in space. It relies on  $k$ -space undersampling and multiple receiver coils with complementary sensitivity profiles in order to reconstruct a full Field-Of-View (FOV) image. The performance of parallel imaging mainly depends on the reconstruction algorithm, which can proceed either in the original  $k$ -space (GRAPPA, SMASH) or in the image domain (SENSE-like methods). To improve the performance of the widely used SENSE algorithm, 2D- or slice-specific regularization in the wavelet domain has been efficiently investigated. In this paper, we extend this approach using 3D-wavelet representations in order to handle all slices together and address reconstruction artifacts which propagate across adjacent slices. The extension also accounts for temporal correlations that exist between successive scans in functional MRI (fMRI). The proposed 4D reconstruction scheme is fully *unsupervised* in the sense that all regularization parameters are estimated in the maximum likelihood sense on a reference scan. The gain induced by such extensions is first illustrated on EPI image reconstruction but also measured in terms of statistical sensitivity during a fast event-related fMRI protocol. The pro-

posed 4D-UWR-SENSE algorithm outperforms the SENSE reconstruction at the subject and group-levels (15 subjects) for different contrasts of interest and using different parallel acceleration factors on  $2 \times 2 \times 3\text{mm}^3$  EPI images.

*Keywords:* pMRI, SENSE, frames, sparsity, fMRI, convex optimization, parallel computing, proximal methods

---

## 1. Introduction

Reducing scanning time in Magnetic Resonance Imaging (MRI) exams remains a worldwide challenging issue. The expected benefits of a faster acquisition can be summarized as follows: i) limit patient's exposure to the MRI environment either for safety or discomfort reasons, ii) maintain a strong robustness in the acquisition with respect to subject's motion artifacts, iii) limit geometric distortions or maintain high image quality and iv) acquire more spatially or temporally resolved images in the same or even reduced amount of time [22, 36]. The basic idea to make MRI acquisitions faster or to improve spatial resolution at fixed scanning time consists of reducing the amount of acquired samples in the  $k$ -space and developing dedicated reconstruction pipelines. To achieve this goal, two main research avenues have been developed so far: i) *parallel imaging* that relies on a geometrical complementarity principle involving multiple receiver channel coils with complementary sensitivity profiles. This enables the reduction of the number of  $k$ -space lines to be acquired without degrading spatial resolution or truncating the Field of View (FOV), and thus requires the combination of reduced FOV coil-specific images to reconstruct the full FOV image [34, 18]. ii) *compressed sensing MRI* that exploits the implicit sparsity in MR images to significantly undersample the  $k$ -space and randomly select incoherent (or complementary) samples regarding their spectral contribution to the MR image [26]. This approach which does not require any multiple channel coil and thus remains useable with birdcage ones will not be addressed in this work.

The present paper is a contribution to parallel imaging at conventional magnetic field strength (e.g. 3 Tesla). At 3 Tesla, Parallel Magnetic Resonance Imaging (pMRI) is mainly useful in reception, i.e. at the image *reconstruction* step using multiple channel coils, while higher magnetic fields (i.e. 7 Tesla) require parallel imaging at the *transmission* step as well [20, 3].

Many methods like GRAPPA (Generalized Autocalibrating Partially Parallel Acquisitions) [18] and SENSE (Sensitivity Encoding) [34] have been

proposed in the literature to reconstruct a full FOV image from multiple  $k$ -space under-sampled images acquired on separate channels. The main difference between these two classes of methods lies in the space on which they operate: GRAPPA performs multichannel full FOV reconstruction in the  $k$ -space whereas SENSE carries out the unfolding process in the image domain: all the under-sampled images are first reconstructed by inverse Fourier transform before combining them to unwrap the full FOV image. Another difference is that GRAPPA is autocalibrated, while SENSE needs a separate coil sensitivity estimation step based on a reference scan. Note however that an autocalibrated version of SENSE is also available for instance in Siemens scanners and called **m**SENSE hereafter. SENSE as well as GRAPPA methods may suffer from strong artifacts when high values of acceleration factors  $R$  are considered in the imaging setup or when they are applied to Echo Planar Imaging (EPI), the sequence involved in fMRI experiments. These artifacts can drastically disturb subsequent statistical analysis such as brain activation detection. Regularized SENSE methods have been proposed in the literature to improve the robustness of the solution [23, 46, 48, 6, 24]. Some of them apply quadratic or Total Variation (TV) regularizations while others resort to regularization in the wavelet transform domain (e.g. UWR-SENSE [7]). The latter strategy has proved its efficiency on the reconstruction of anatomical or functional (resting-state only) data [6, 7]. More recently, UWR-SENSE has been assessed on EPI images and compared with **m**SENSE on the same data acquired during a brain activation fMRI experiment [5]. This comparison was performed at the subject level on a few subjects only.

Besides, most of the available reconstruction methods in the literature operate slice by slice and thus reconstruct each slice irrespective of its neighbors. Iterating over slices is thus necessary to get the whole 3D volume. This observation led us to consider 3D or whole brain reconstruction as a single step in which all slices are treated together by making use of 3D wavelet transforms and 3D sparsity promoting regularization terms in the wavelet domain. Following the same principle, an fMRI run usually consists of several hundred successive scans that are reconstructed independently one to another and thus implicitly assumed to be independent of each other. Iterating over all acquired 3D volumes remains the classical approach to reconstruct the 4D or 3D +  $t$  dataset associated with an fMRI run. However, it has been shown for a long while that fMRI data are serially correlated in time even under the null hypothesis (i.e., ongoing activity only) [1, 47, 35]. To capture this dependence between successive time points, an autoregressive model has

demonstrated its relevance [44, 45, 31], especially when its parameters and optimal order can vary in space for instance with tissue type [43, 30]. Hence, it makes sense to account for this temporal structure at the reconstruction step.

These two key ideas play a central role in the present paper by extending the UWR-SENSE approach [7] through a fidelity data term combining all time points, which relies on a 3D wavelet transform and an additional regularization term along the temporal dimension of the 4D dataset in the image domain. The development of the proposed method (named 4D-UWR-SENSE) was made possible due to recent advances in nonsmooth convex optimization. Indeed, it is based on a Parallel ProXimal Algorithm (PPXA) which is different from the ones employed in [7].

4D-UWR-SENSE leads to improvements in the retrieval of a reliable Signal-to-Noise Ratio (SNR) between the acquired volumes and also in the enhancement of the detection of BOLD effects or evoked activations that occur in response to the delivered stimuli in the fMRI experiment. The present paper therefore aims at demonstrating that the 4D-UWR-SENSE approach outperforms its SENSE-like alternatives not only in terms of reduced artifacts, but also in terms of statistical sensitivity at the voxel and cluster levels, in intra-subject and group studies. The rest of this paper is organized as follows. Section 2 recalls the general parallel MRI framework. We then describe the proposed reconstruction algorithm in Section 3 before illustrating related experimental results in Section 4. Finally, some discussions and conclusions are drawn in Section 5.

## 2. Parallel imaging in MRI

In parallel MRI, an array of  $L$  coils is employed to measure the spin density  $\bar{\rho}$  into the object under investigation<sup>1</sup>. The signal  $\tilde{d}_\ell$  received by each coil  $\ell$  ( $1 \leq \ell \leq L$ ) is the Fourier transform of the desired 2D field  $\bar{\rho} \in \mathbb{R}^{X \times Y}$  on the specified FOV weighted by the coil sensitivity profile  $s_\ell$ , evaluated at some location  $\mathbf{k}_r = (k_x, k_y)^\top$  in the  $k$ -space:

$$\tilde{d}_\ell(\mathbf{k}_r) = \int \bar{\rho}(\mathbf{r}) s_\ell(\mathbf{r}) e^{-i2\pi \mathbf{k}_r^\top \mathbf{r}} d\mathbf{r} + \tilde{n}_\ell(\mathbf{k}_r), \quad (1)$$

where  $\tilde{n}_\ell(\mathbf{k}_r)$  is a coil-dependent additive zero-mean Gaussian noise, which is independent and identically distributed (iid) in the  $k$ -space, and  $\mathbf{r} = (x, y)^\top \in$

---

<sup>1</sup>The overbar is used to distinguish the “true” data from a generic variable.

$X \times Y$  is the spatial position in the image domain ( $\cdot^\top$  being the transpose operator). The size of the reduced FOV acquired data  $\tilde{d}_\ell$  in the  $k$ -space clearly depends on the sampling scheme. In contrast with cardiac imaging where the heart motion is significant during scanning, a Cartesian coordinate system is generally adopted in the neuroimaging context. In parallel MRI, the sampling period along the phase encoding direction is  $R$  times larger than the one used for conventional acquisition,  $R \leq L$  being the reduction factor. To recover full FOV images, many algorithms have been proposed but only SENSE-like [33] and GRAPPA-like [18] methods are provided by scanner manufacturers. In what follows, we focus on SENSE-like methods operating in the spatial domain.

Let  $\Delta y = \frac{Y}{R}$  be the aliasing period and  $y$  the position in the image domain along the phase encoding direction. Let  $x$  be the position in the image domain along the frequency encoding direction. A 2D inverse Fourier transform allows us to recover the measured signal in the spatial domain. By accounting for the  $k$ -space undersampling at  $R$ -rate, the inverse Fourier transform gives us the spatial counterpart of Eq. (1) in matrix form:

$$\mathbf{d}(\mathbf{r}) = \mathbf{S}(\mathbf{r})\bar{\boldsymbol{\rho}}(\mathbf{r}) + \mathbf{n}(\mathbf{r}), \quad (2)$$

where

$$\mathbf{S}(\mathbf{r}) \triangleq \begin{bmatrix} s_1(x, y) & \dots & s_1(x, y + (R-1)\Delta y) \\ \vdots & \vdots & \vdots \\ s_L(x, y) & \dots & s_L(x, y + (R-1)\Delta y) \end{bmatrix}, \quad \mathbf{n}(\mathbf{r}) \triangleq \begin{bmatrix} n_1(x, y) \\ n_2(x, y) \\ \vdots \\ n_L(x, y) \end{bmatrix}$$

$$\bar{\boldsymbol{\rho}}(\mathbf{r}) \triangleq \begin{bmatrix} \bar{\rho}(x, y) \\ \bar{\rho}(x, y + \Delta y) \\ \vdots \\ \bar{\rho}(x, y + (R-1)\Delta y) \end{bmatrix} \quad \text{and} \quad \mathbf{d}(\mathbf{r}) \triangleq \begin{bmatrix} d_1(x, y) \\ d_2(x, y) \\ \vdots \\ d_L(x, y) \end{bmatrix}. \quad (3)$$

Based upon this model, the reconstruction step consists of solving Eq. (2) so as to recover  $\bar{\boldsymbol{\rho}}(\mathbf{r})$  from  $\mathbf{d}(\mathbf{r})$  and an estimate of  $\bar{\mathbf{S}}(\mathbf{r})$  at each spatial position  $\mathbf{r} = (x, y)^\top$ . The spatial mixture or *sensitivity* matrix  $\bar{\mathbf{S}}(\mathbf{r})$  is estimated

using a reference scan and varies according to the coil geometry. Note that the coil images  $(d_\ell)_{1 \leq \ell \leq L}$  as well as the sought image  $\bar{\rho}$  are complex-valued, although  $|\bar{\rho}|$  is only considered for visualization purposes. The next section describes the widely used SENSE algorithm as well as its regularized extensions.

### 3. Reconstruction algorithms

#### 3.1. 1D-SENSE

In its simplest form, SENSE imaging amounts to solving a one-dimensional inversion problem due to the separability of the Fourier transform. Note however that this inverse problem admits a two-dimensional extension in 3D imaging sequences like Echo Volume Imaging (EVI) [36] where under-sampling occurs in two  $k$ -space directions. The 1D-SENSE reconstruction method [33] actually minimizes a Weighted Least Squares (WLS) criterion  $\mathcal{J}_{\text{WLS}}$  given by:

$$\mathcal{J}_{\text{WLS}}(\rho) = \sum_{\mathbf{r} \in \{1, \dots, X\} \times \{1, \dots, Y/R\}} \|\mathbf{d}(\mathbf{r}) - \mathbf{S}(\mathbf{r})\rho(\mathbf{r})\|_{\Psi^{-1}}^2, \quad (4)$$

where  $\|\cdot\|_{\Psi^{-1}} = \sqrt{(\cdot)^{\text{H}}\Psi^{-1}(\cdot)}$ , and the noise covariance matrix  $\Psi$  is usually estimated based on  $L$  acquired images  $(\underline{d}_\ell)_{1 \leq \ell \leq L}$  from all coils without radio frequency pulse. Hence, the SENSE full FOV image is nothing but the maximum likelihood estimate under Gaussian noise assumption, which admits the following closed-form expression at each spatial position  $\mathbf{r}$ :

$$\hat{\rho}_{\text{WLS}}(\mathbf{r}) = (\mathbf{S}^{\text{H}}(\mathbf{r})\Psi^{-1}\mathbf{S}(\mathbf{r}))^{\#} \mathbf{S}^{\text{H}}(\mathbf{r})\Psi^{-1}\mathbf{d}(\mathbf{r}), \quad (5)$$

where  $(\cdot)^{\text{H}}$  (resp.  $(\cdot)^{\#}$ ) stands for the transposed complex conjugate (resp. pseudo-inverse). It should be noticed here that the described 1D-SENSE reconstruction method has been designed to reconstruct one slice (2D image). To reconstruct a full volume, the 1D-SENSE reconstruction algorithm has to be iterated over all slices.

In practice, the performance of the 1D-SENSE method is limited because of *i*) the presence of distortions in the measurements  $\mathbf{d}(\mathbf{r})$ , *ii*) the ill-conditioning of  $\mathbf{S}(\mathbf{r})$ , in particular at locations  $\mathbf{r}$  close to the image center and *iii*) the presence of errors in the estimation of  $\mathbf{S}(\mathbf{r})$  mainly at brain/air interfaces. To enhance the robustness of the solution to this ill-posed problem, a regularization is usually introduced in the reconstruction process. To improve results obtained with quadratic regularization techniques [23, 46], edge-preserving

regularization has been widely investigated in the pMRI reconstruction literature. For instance, reconstruction methods based on Total Variation (TV) regularization have been proposed in a number of recent works like [21, 25]. However, TV is mostly adapted to piecewise constant images, which are not always accurate models in MRI, especially in fMRI. As investigated by *Chaari et al.* [7] and *Liu et al.* [24], regularization in the Wavelet Transform (WT) domain is a powerful tool to improve SENSE reconstruction. In what follows, we summarize the principles of the wavelet-based regularization approach.

### 3.2. Proposed wavelet Regularized-SENSE

Akin to [7] where a regularized reconstruction algorithm relying on 2D separable WTs was investigated, to the best of our knowledge, all the existing approaches in the pMRI regularization literature proceed slice by slice. The drawback of this strategy is that no spatial continuity between adjacent slices is taken into account since the slices are processed independently. Moreover, since the whole brain volume has to be acquired several times in an fMRI study, iterating over all the acquired 3D volumes is then necessary in order to reconstruct a 4D data volume corresponding to an fMRI session. Consequently, the 3D volumes are supposed independent whereas fMRI time-series are serially correlated in time because of two distinct effects: the BOLD signal itself is a low-pass filtered version of the neural activity, and physiological artifacts make the fMRI time points strongly dependent. For these reasons, modeling temporal dependence across scans at the reconstruction step may impact subsequent statistical analysis. This has motivated the extension of the wavelet regularized reconstruction approach in [7] in order to:

- account for 3D spatial dependencies between adjacent slices by using 3D WTs,
- exploit the temporal dependency between acquired 3D volumes by applying an additional regularization term along the temporal dimension of the 4D dataset.

This additional regularization will help in increasing the Signal to Noise Ratio (SNR) through the acquired volumes, and therefore enhance the reliability of the statistical analysis in fMRI. These temporal dependencies have also been used in the dynamic MRI literature in order to improve the reconstruction quality in conventional MRI [39]. However, since the imaged object

geometry in the latter context generally changes during the acquisition, taking into account the temporal regularization in the reconstruction process is very difficult.

To deal with a 4D reconstruction of the  $N_r$  acquired volumes, we will first rewrite the observation model in Eq. (2) as follows:

$$\mathbf{d}^t(\mathbf{r}) = \mathbf{S}(\mathbf{r})\boldsymbol{\rho}^t(\mathbf{r}) + \mathbf{n}^t(\mathbf{r}), \quad (6)$$

where  $t \in \{1, \dots, N_r\}$  is the acquisition time and  $\mathbf{r} = (x, y, z)$  is the 3D spatial position,  $z \in \{1, \dots, Z\}$  being the position along the third direction (slice selection one).

At a given time  $t$ , the full FOV 3D complex-valued image  $\bar{\rho}^t$  of size  $X \times Y \times Z$  can be seen as an element of the Euclidean space  $\mathbb{C}^K$  with  $K = X \times Y \times Z$  endowed with the standard inner product  $\langle \cdot | \cdot \rangle$  and norm  $\| \cdot \|$ . We employ a dyadic 3D orthonormal wavelet decomposition operator  $T$  over  $j_{\max}$  resolution levels. The coefficient field resulting from the wavelet decomposition of a target image  $\rho^t$  is defined as  $\zeta^t = (\boldsymbol{\zeta}_a^t, (\boldsymbol{\zeta}_{o,j}^t)_{o \in \mathbb{O}, 1 \leq j \leq j_{\max}})$  with  $o \in \mathbb{O} = \{0, 1\}^3 \setminus \{(0, 0, 0)\}$ ,  $\boldsymbol{\zeta}_a^t = (\zeta_{a,k}^t)_{1 \leq k \leq K_{j_{\max}}}$  and  $\boldsymbol{\zeta}_{o,j}^t = (\zeta_{o,j,k}^t)_{1 \leq k \leq K_j}$  where  $K_j = K2^{-3j}$  is the number of wavelet coefficients in a given subband at resolution  $j$  (by assuming that  $X, Y$  and  $Z$  are multiple of  $2^{j_{\max}}$ ). Adopting such a notation, the wavelet coefficients have been reindexed so that  $\boldsymbol{\zeta}_a^t$  denotes the approximation coefficient vector at the resolution level  $j_{\max}$ , while  $\boldsymbol{\zeta}_{o,j}^t$  denotes the detail coefficient vector at the orientation  $o$  and resolution level  $j$ . Using 3D dyadic WTs allows us to smooth reconstruction artifacts along the slice selection direction, which is not possible using a slice by slice operating approach.

The proposed regularization procedure relies on the introduction of two penalty terms. The first penalty term describes the prior spatial knowledge about the wavelet coefficients of the target solution and it is expressed as:

$$g(\zeta) = \sum_{t=1}^{N_r} \left[ \sum_{k=1}^{K_{j_{\max}}} \Phi_a(\zeta_{a,k}^t) + \sum_{o \in \mathbb{O}} \sum_{j=1}^{j_{\max}} \sum_{k=1}^{K_j} \Phi_{o,j}(\zeta_{o,j,k}^t) \right], \quad (7)$$

where  $\zeta = (\zeta^1, \zeta^2, \dots, \zeta^{N_r})$  and we have, for every  $o \in \mathbb{O}$  and  $j \in \{1, \dots, j_{\max}\}$ ,

$$\forall \xi \in \mathbb{C}, \quad \Phi_{o,j}(\xi) = \Phi_{o,j}^{\text{Re}}(\xi) + \Phi_{o,j}^{\text{Im}}(\xi) \quad (8)$$

where  $\Phi_{o,j}^{\text{Re}}(\xi) = \alpha_{o,j}^{\text{Re}}|\text{Re}(\xi - \mu_{o,j})| + \frac{\beta_{o,j}^{\text{Re}}}{2}|\text{Re}(\xi - \mu_{o,j})|^2$  and  $\Phi_{o,j}^{\text{Im}}(\xi) = \alpha_{o,j}^{\text{Im}}|\text{Im}(\xi - \mu_{o,j})| + \frac{\beta_{o,j}^{\text{Im}}}{2}|\text{Im}(\xi - \mu_{o,j})|^2$  with  $\mu_{o,j} = \mu_{o,j}^{\text{Re}} + \imath\mu_{o,j}^{\text{Im}} \in \mathbb{C}$ , and  $\alpha_{o,j}^{\text{Re}}, \beta_{o,j}^{\text{Re}}, \alpha_{o,j}^{\text{Im}}, \beta_{o,j}^{\text{Im}}$  are some positive real constants. Hereabove,  $\text{Re}(\cdot)$  and  $\text{Im}(\cdot)$  (or  $\cdot^{\text{Re}}$  and  $\cdot^{\text{Im}}$ ) stand for the real and imaginary parts, respectively. A similar model is adopted for the approximation coefficients. The second regularization term penalizes the temporal variation between successive 3D volumes:

$$h(\zeta) = \kappa \sum_{t=2}^{N_r} \|T^* \zeta^t - T^* \zeta^{t-1}\|_p^p \quad (9)$$

where  $T^*$  is the 3D wavelet reconstruction operator. The prior parameters  $\boldsymbol{\alpha}_{o,j} = (\alpha_{o,j}^{\text{Re}}, \alpha_{o,j}^{\text{Im}})$ ,  $\boldsymbol{\beta}_{o,j} = (\beta_{o,j}^{\text{Re}}, \beta_{o,j}^{\text{Im}})$ ,  $\boldsymbol{\mu}_{o,j} = (\mu_{o,j}^{\text{Re}}, \mu_{o,j}^{\text{Im}})$ ,  $\kappa \in \mathbb{R}_+$  and  $p \in [1, +\infty[$  are unknown and they need to be estimated (see Appendix A).

The operator  $T^*$  is then applied to each component  $\zeta^t$  of  $\zeta$  to obtain the reconstructed 3D volume  $\rho^t$  related to the acquisition time  $t$ . It should be noticed here that other choices for the penalty functions are also possible provided that the convexity of the resulting optimality criterion is ensured. This condition enables the use of fast and efficient convex optimization algorithms. Adopting this formulation, the minimization process plays a prominent role in the reconstruction process, as detailed in Appendix B.

#### 4. Experimental validation in fMRI

This section is dedicated to the experimental validation of the 4D-UWR-SENSE reconstruction algorithm we proposed in Section 3.2. Results of subject and group-level fMRI statistical analyses are compared for two reconstruction pipelines: one available on the Siemens workstation and our own pipeline involving for the sake of completeness either the early UWR-SENSE [7] or the 4D-UWR-SENSE version of the proposed pMRI reconstruction algorithm. In what follows, we first describe the fMRI acquisition setup and the experimental design.

##### 4.1. Experimental data

For validation purpose, we acquired fMRI data on a 3 T Siemens Trio magnet using a Gradient-Echo EPI (GE-EPI) sequence ( $TE = 30$  ms,  $TR = 2400$  ms, slice thickness = 3 mm, transversal orientation,  $FOV = 192$  mm<sup>2</sup>) during a cognitive *localizer* [32] protocol. This experiment has been designed

to map auditory, visual and motor brain functions as well as higher cognitive tasks such as number processing and language comprehension (listening and reading). It consisted of a single session of  $N_r = 128$  scans. The paradigm was a fast event-related design comprising sixty auditory, visual and motor stimuli, defined in ten experimental conditions (auditory and visual sentences, auditory and visual calculations, left/right auditory and visual clicks, horizontal and vertical checkerboards). An  $L = 32$  channel coil was used to enable parallel imaging. Ethics approval was given by the local research ethics committee, and fifteen subjects gave written informed consent for participation. For each subject, fMRI data were collected at the  $2 \times 2 \text{ mm}^2$  spatial in-plane resolution using different reduction factors ( $R = 2$  or  $R = 4$ ). Based on the raw data files delivered by the scanner, reduced FOV EPI images were reconstructed as detailed in Fig. 1. This reconstruction requires two specific treatments:

- i)  $k$ -space regridding* to account for the non-uniform  $k$ -space sampling during readout gradient ramp, which occurs in fast MRI sequences like GE-EPI;
- ii) Nyquist ghosting correction* to remove the odd-even echo inconsistencies during  $k$ -space acquisition of EPI images.

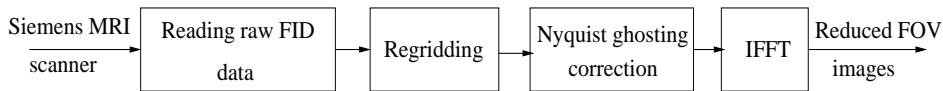


Figure 1: Reconstruction pipeline of reduced FOV EPI images from the raw FID data.

Once the reduced FOV images are available, the proposed pMRI 4D-UWR-SENSE algorithm and its early UWR-SENSE version have been utilized in a final step to reconstruct the full FOV EPI images and compared to the mSENSE<sup>2</sup> Siemens solution. For the wavelet-based regularization, dyadic ( $M = 2$ ) *Symmlet* orthonormal wavelet bases [15] associated with filters of length 8 have been used over  $j_{\max} = 3$  resolution levels. The reconstructed EPI images then enter in our fMRI study in order to measure the impact of the reconstructor choice on brain activity detection. Note also that the proposed reconstruction algorithm requires the estimation of the coil sensitivity

---

<sup>2</sup>SENSE reconstruction implemented by the Siemens scanner

maps (matrix  $\mathbf{S}(\cdot)$  in Eq. (2)). As proposed in [34], the latter were estimated by dividing the coil-specific images by the module of the Sum Of Squares (SOS) images, which are computed from the specific acquisition of the  $k$ -space center (24 lines) before the  $N_r$  scans.

Fig. 2 compares the two pMRI reconstruction algorithms to illustrate on axial, coronal and sagittal slices how the mSENSE reconstruction artifacts have been removed using the 4D-UWR-SENSE approach. The mSENSE reconstructed images acutally present large artifacts located both at the center and boundaries of the brain in sensory and cognitive regions (temporal lobes, frontal and motor cortices, ...). This results in SNR loss and thus may have a dramatic impact for activation detection in these brain regions. Note that these conclusions are reproducible across subjects although the artifacts may appear on different slices (see red circles in Fig.2). It is also worth mentioning that in contrast to the Siemens reconstructor our pipeline does not involve any spatial filtering step to improve signal homogeneity across the brain: this explains why the images shown in Fig. 2 and delivered by our 4D-UWR-SENSE algorithm seem less homogeneous. However, bias field correction can be applied if necessary using specific tools such as those available in BrainVISA<sup>3</sup>.

Regarding the computation burden, the mSENSE algorithm is carried out on-line and remains compatible with real time processing. On the other hand, our pipeline is carried out off-line and requires much more computation. For illustration purpose, on a biprocessor quadicore Intel Xeon CPU@ 2.67GHz, one EPI slice is reconstructed in 4 s using the UWR-SENSE algorithm. Using parallel computing strategy and multithreading (through the OMP library), each EPI volume consisting of 40 slices is reconstructed in 22 s. This makes the whole series of 128 EPI images available in about 47 min. In contrast, the proposed 4D-UWR-SENSE achieves the reconstruction of the series in about 40 min, but requires larger memory space due to large data volume processed simultaneously.

#### 4.2. fMRI data pre-processings

Irrespective of the reconstruction pipeline, the full FOV fMRI images were then preprocessed using the SPM5 software<sup>4</sup>: preprocessing involves

---

<sup>3</sup><http://brainvisa.info>.

<sup>4</sup><http://www.fil.ion.ucl.ac.uk/spm/software/spm5/>

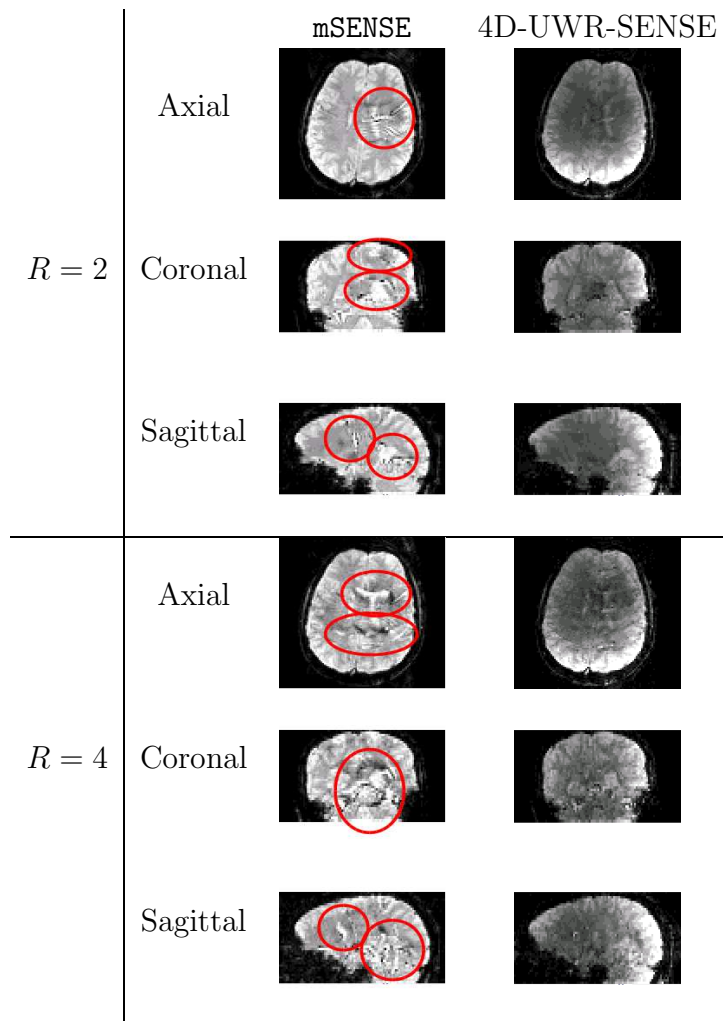


Figure 2: **Axial**, **Coronal** and **Sagittal** reconstructed slices using mSENSE and 4D-UWR-SENSE for  $R = 2$  and  $R = 4$  with  $2 \times 2 \text{ mm}^2$  in-plane spatial resolution. Red circles and ellipsoids indicate the position of reconstruction artifacts using mSENSE.

realignment, correction for motion and differences in slice acquisition time, spatial normalization, and smoothing with an isotropic Gaussian kernel of 4mm full-width at half-maximum. Anatomical normalization to MNI space was performed by coregistration of the functional images with the anatomical T1 scan acquired with the thirty two channel-head coil. Parameters for the normalization to MNI space were estimated by normalizing this scan to the T1 MNI template provided by SPM5, and were subsequently applied to all

functional images.

### 4.3. Subject-level analysis

A General Linear Model (GLM) was constructed to capture stimulus-related BOLD response. As shown in Fig. 3, the design matrix relies on ten experimental conditions and thus made up of twenty one regressors corresponding to stick functions convolved with the canonical Haemodynamic Response Function (HRF) and its first temporal derivative, the last regressor modelling the baseline. This GLM was then fitted to the same acquired images but reconstructed using either the Siemens reconstructor or our own pipeline, which in the following is derived from the early UWR-SENSE method [7] and from its 4D-UWR-SENSE extension we propose here.

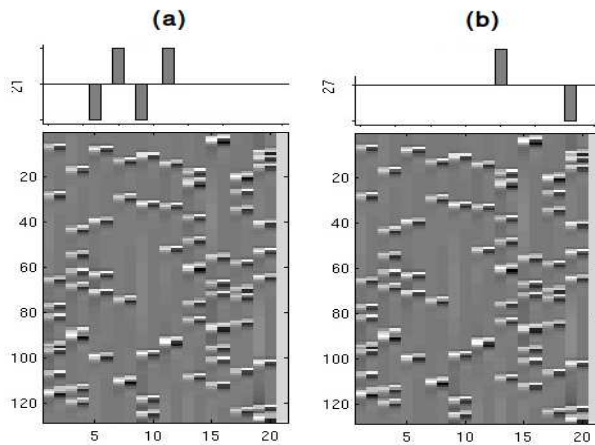


Figure 3: (a): design matrix and the Lc-Rc contrast involving two conditions (grouping auditory and visual modalities); (b): design matrix and the aC-aS contrast involving four conditions (sentence, computation, left click, right click).

Here, contrast estimate images for motor responses and higher cognitive functions (computation, language) were subjected to further analyses at the subject and group levels. These two contrast are complementary since the expected activations lie in different brain regions and thus can be differentially corrupted by reconstruction artifacts as outlined in Fig. 2. More precisely, we studied:

- the **Auditory computation vs. Auditory sentence (aC-aS)** contrast which is supposed to elicit evoked activity in the frontal and pari-

etal lobes, since solving mental arithmetic task involves working memory and more specifically the intra-parietal sulcus [16]: see Fig. 3(b);

- the **Left click vs. Right click** (Lc-Rc) contrast for which we expect evoked activity in the right motor cortex (precentral gyrus, middle frontal gyrus). Indeed, the Lc-Rc contrast defines a compound comparison which involves two motor stimuli which are presented either in the visual or auditory modality. This comparison aims therefore at detecting lateralization effect in the motor cortex: see Fig. 3(a).

Interestingly, these two contrasts were chosen because they summarized well different situations (large vs small activation clusters, distributed vs focal activation pattern, bilateral vs unilateral activity) that occurred for this paradigm when looking at sensory areas (visual, auditory, motor) or regions involved in higher cognitive functions (reading, calculation). In the following, our results are reported in terms of Student- $t$  maps thresholded at a cluster-level  $p = 0.05$  corrected for multiple comparisons according to the FamilyWise Error Rate (FWER) [29, 4]. Complementary statistical tables provide corrected cluster and voxel-level  $p$ -values, maximal  $t$ -scores and corresponding peak positions both for  $R = 2$  and  $R = 4$ . Note that clusters are listed in a decreasing order of significance.

Concerning the aC-aS contrast, Fig. 4[top] shows for the most significant slice and  $R = 2$  that all pMRI reconstruction algorithms succeed in finding evoked activity in the left parietal and frontal cortices, more precisely in the inferior parietal lobule and middle frontal gyrus according to the AAL template<sup>5</sup>. Table 1 also confirms a bilateral activity pattern in parietal regions for  $R = 2$ . Moreover, for  $R = 4$  Fig. 4[bottom] illustrates that our pipeline (UWR-SENSE and 4D-UWR-SENSE) and preferentially the proposed 4D-UWR-SENSE scheme enables to retrieve reliable frontal activity elicited by mental calculation, which is lost by the the mSENSE algorithm. From a quantitative viewpoint, the proposed 4D-UWR-SENSE algorithm finds larger clusters whose local maxima are more significant than the ones obtained using mSENSE and UWR-SENSE, as reported in Table 1. Concerning the most significant cluster for  $R = 2$ , the peak positions remain stable whatever the reconstruction algorithm. However, examining their significance level, one can first measure the benefits of wavelet-based

---

<sup>5</sup>available in the xjView toolbox of SPM5.

regularization when comparing UWR-SENSE with mSENSE results and then additional positive effects of temporal regularization and 3D wavelet decomposition when looking at the 4D-UWR-SENSE results. These benefits are also demonstrated for  $R = 4$ .

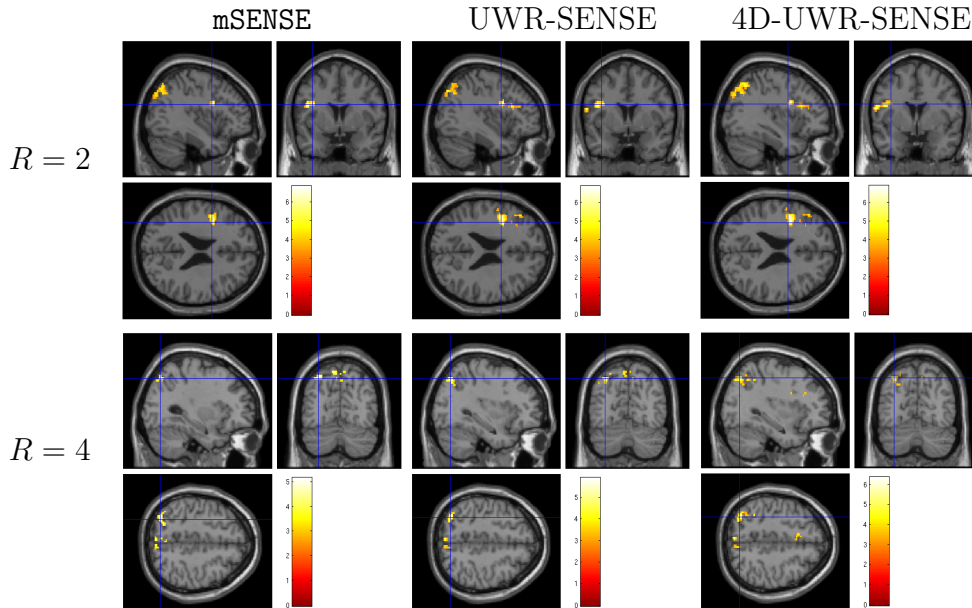


Figure 4: Subject-level student- $t$  maps superimposed to anatomical MRI for the ac-aS contrast. Data have been reconstructed using the mSENSE, UWR-SENSE and 4D-UWR-SENSE, respectively. Neurological convention: **left is left**. The blue cross shows the maximum activation peak.

Fig. 5 illustrates another property of the proposed pMRI pipeline, ie its robustness to the between-subject variability. Indeed, when comparing subject-level student- $t$  maps reconstructed using the different pipelines ( $R = 2$ ), it can be observed that the mSENSE algorithm fails to detect any activation cluster in the expected regions for the second subject (see Fig. 5[bottom]). In contrast, our 4D-UWR-SENSE method retrieves more coherent activity while not exactly at the same position as for the first subject.

For the Lc-Rc contrast on the data acquired with  $R = 2$ , Fig. 6[top] shows that all reconstruction methods enable to retrieve expected activation in the right precentral gyrus. However, when looking more carefully at the statistical results (see Table 2), our pipeline and more preferentially the 4D-UWR-SENSE algorithm retrieves an additional cluster in the right middle frontal gyrus. On data acquired with  $R = 4$ , the same Lc-Rc contrast elicits

Table 1: Significant statistical results at the subject-level for the aC-aS contrast (corrected for multiple comparisons at  $p = 0.05$ ). Images were reconstructed using the mSENSE, UWR-SENSE and 4D-UWR-SENSE algorithm for  $R = 2$  and  $R = 4$ .

|         |              | cluster-level |            | voxel-level |             |            |
|---------|--------------|---------------|------------|-------------|-------------|------------|
|         |              | p-value       | Size       | p-value     | T-score     | Position   |
| $R = 2$ | mSENSE       | $< 10^{-3}$   | 320        | $< 10^{-3}$ | 6.40        | -32 -76 45 |
|         |              | $< 10^{-3}$   | 163        | $< 10^{-3}$ | 5.96        | -4 -70 54  |
|         |              | $< 10^{-3}$   | 121        | $< 10^{-3}$ | 6.34        | 34 -74 39  |
|         |              | $< 10^{-3}$   | 94         | $< 10^{-3}$ | 6.83        | -38 4 24   |
|         | UWR-SENSE    | $< 10^{-3}$   | 407        | $< 10^{-3}$ | 6.59        | -32 -76 45 |
|         |              | $< 10^{-3}$   | 164        | $< 10^{-3}$ | 5.69        | -6 -70 54  |
|         |              | $< 10^{-3}$   | 159        | $< 10^{-3}$ | 5.84        | 32 -70 39  |
|         |              | $< 10^{-3}$   | 155        | $< 10^{-3}$ | 6.87        | -44 4 24   |
|         | 4D-UWR-SENSE | $< 10^{-3}$   | <b>454</b> | $< 10^{-3}$ | 6.54        | -32 -76 45 |
|         |              | $< 10^{-3}$   | 199        | $< 10^{-3}$ | 5.43        | -6 26 21   |
|         |              | $< 10^{-3}$   | 183        | $< 10^{-3}$ | 5.89        | 32 -70 39  |
|         |              | $< 10^{-3}$   | 170        | $< 10^{-3}$ | <b>6.90</b> | -44 4 24   |
| $R = 4$ | mSENSE       | $< 10^{-3}$   | 58         | 0.028       | 5.16        | -30 -72 48 |
|         | 4D-UWR-SENSE | $< 10^{-3}$   | 94         | 0.003       | 5.91        | -32 -70 48 |
|         |              | $< 10^{-3}$   | 60         | 0.044       | 4.42        | -6 -72 54  |
|         | 4D-UWR-SENSE | $< 10^{-3}$   | <b>152</b> | $< 10^{-3}$ | <b>6.36</b> | -32 -70 48 |
|         |              | $< 10^{-3}$   | 36         | 0.009       | 5.01        | -4 -78 48  |
|         |              | $< 10^{-3}$   | 29         | 0.004       | 5.30        | -34 6 27   |

similar activations, ie in the same region. As demonstrated in Fig. 6[bottom], this activity is enhanced when pMRI reconstruction is performed with our pipeline. Quantitative results in Table 2 confirms numerically what can be observed in Fig. 6: larger clusters with higher local  $t$ -scores are detected using the 4D-UWR-SENSE algorithm, both for  $R = 2$  and  $R = 4$ . Also, a larger number of clusters is retrieved for  $R = 2$  using wavelet-based regularization.

Fig. 7 reports on the robustness of the proposed pMRI pipeline to the between-subject variability for this motor contrast. Since sensory functions are expected to generate larger BOLD effects (higher SNR) and appears more stable, our comparison takes place at  $R = 4$ . Two subject-level student- $t$  maps reconstructed using the different pMRI algorithms are compared: in Fig. 7. For the second subject, one can observe that the mSENSE algorithm fails to detect any activation cluster in the right motor cortex. In contrast,

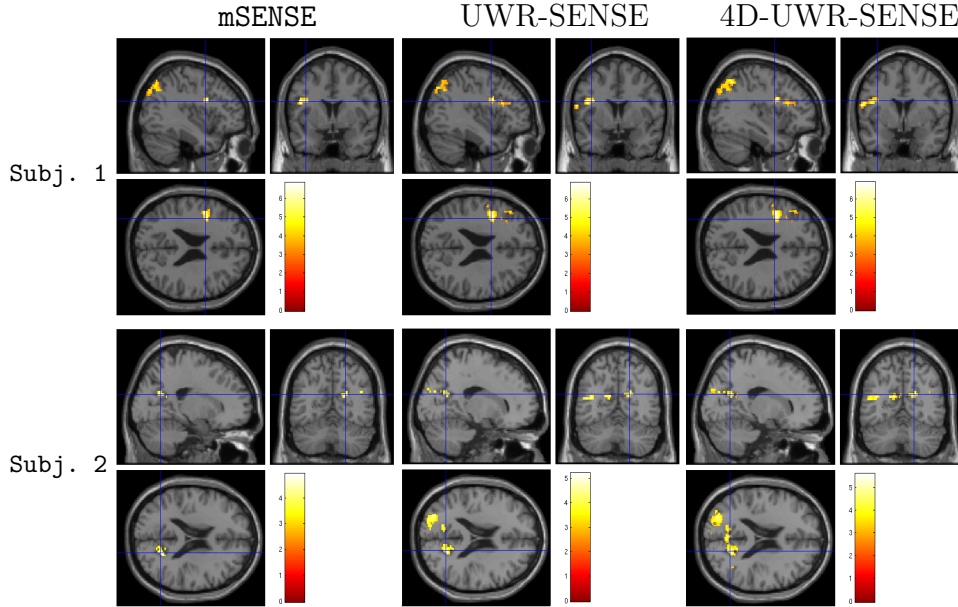


Figure 5: Between-subject variability of detected activation for the aC-aS contrast at  $R = 2$ . Neurological convention. The blue cross shows the activation peak.

Table 2: Significant statistical results at the subject-level for the Lc-Rc contrast (corrected for multiple comparisons at  $p = 0.05$ ). Images were reconstructed using the mSENSE, UWR-SENSE and 4D-UWR-SENSE algorithms for  $R = 2$  and  $R = 4$ .

|         |              | cluster-level |            | voxel-level |             |           |
|---------|--------------|---------------|------------|-------------|-------------|-----------|
|         |              | p-value       | Size       | p-value     | T-score     | Position  |
| $R = 2$ | mSENSE       | $< 10^{-3}$   | 79         | $< 10^{-3}$ | 6.49        | 38 -26 66 |
|         | UWR-SENSE    | $< 10^{-3}$   | 144        | 0.004       | 5.82        | 40 -22 63 |
|         |              | 0.03          | 21         | 0.064       | 4.19        | 24 -8 63  |
|         | 4D-UWR-SENSE | $< 10^{-3}$   | <b>172</b> | 0.001       | <b>6.78</b> | 34 -24 69 |
|         |              | $< 10^{-3}$   | 79         | 0.001       | 6.49        | 38 -26 66 |
| $R = 4$ | mSENSE       | 0.006         | 21         | 0.295       | 4.82        | 34 -28 63 |
|         | UWR-SENSE    | $< 10^{-3}$   | 33         | 0.120       | 5.06        | 40 -24 66 |
|         | 4D-UWR-SENSE | $< 10^{-3}$   | <b>51</b>  | 0.006       | <b>5.57</b> | 40 -24 66 |

our 4D-UWR-SENSE method retrieves more coherent activity for this second subject in the expected region.

To summarize, on these two contrasts our 4D-UWR-SENSE algorithm always outperforms the alternative reconstruction methods in terms of sta-

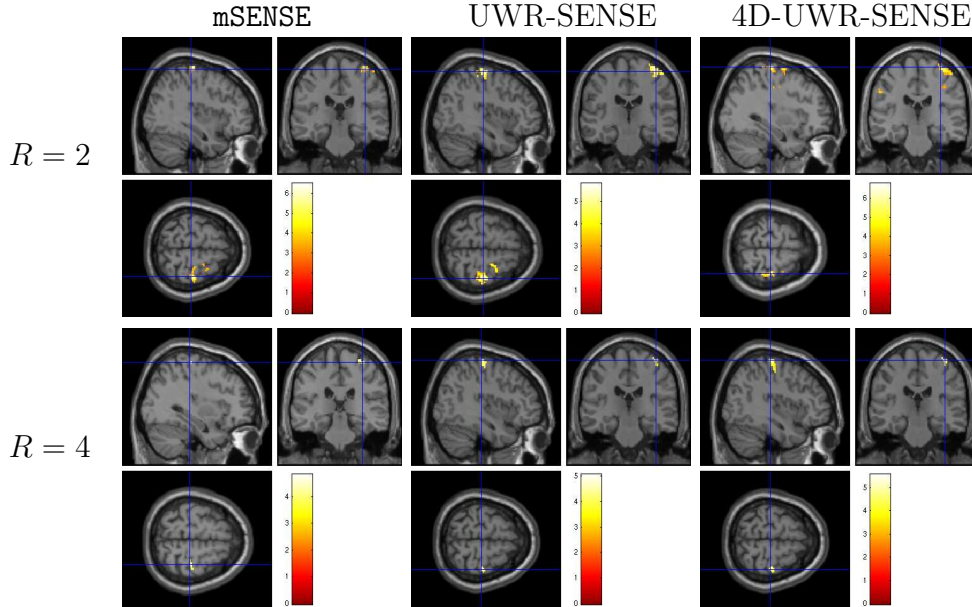


Figure 6: Subject-level student- $t$  maps superimposed to anatomical MRI for the Lc-Rc contrast. Data have been reconstructed using the mSENSE, UWR-SENSE and 4D-UWR-SENSE, respectively. Neurological convention. The blue cross shows the activation peak.

tistical significance (number of clusters, cluster extent, peak values,...) but also in terms of robustness.

#### 4.4. Group-level analysis

Due to between-subject anatomical and functional variability, group-level analysis is necessary in order to derive robust and reproducible conclusions at the population level. For this validation, random effect analyses (RFX) involving fifteen healthy subjects have been conducted on the contrast maps we previously investigated at the subject level. More precisely, one-sample Student- $t$  test was performed on the subject-level contrast images (eg, Lc-Rc, aC-aS,... images) using SPM5.

For the aC-aS contrast, Maximum Intensity Projection (MIP) student- $t$  maps are shown in Fig. 8. First, they illustrate that irrespective of the reconstruction method larger and more significant activations are found on datasets acquired with  $R = 2$  given the better SNR. Second, for  $R = 2$ , visual inspection of Fig. 8[top] confirms that only the 4D-UWR-SENSE algorithm allows us to retrieve significant bilateral activations in the parietal

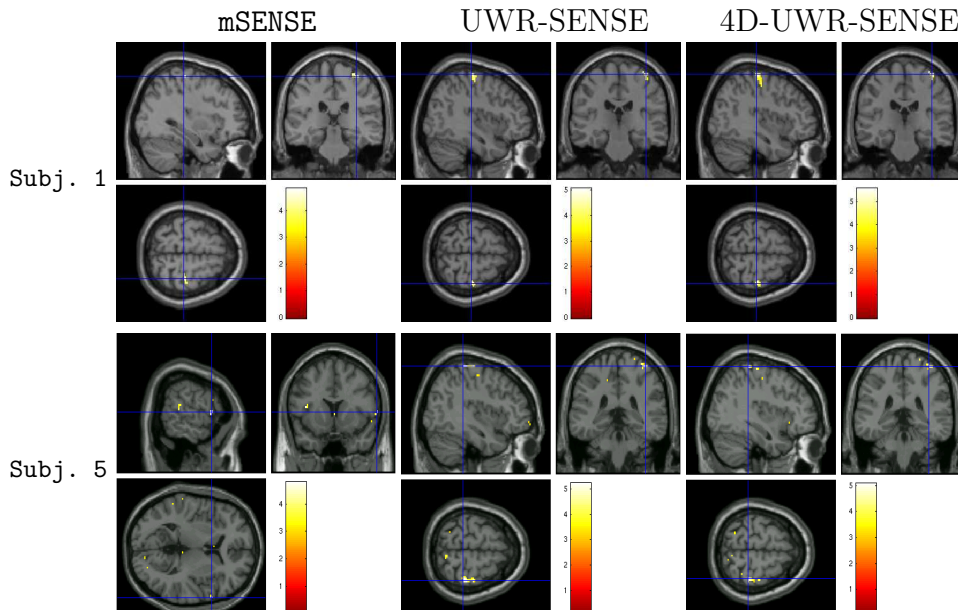


Figure 7: Between-subject variability of detected activation for the Lc-Rc contrast at  $R = 4$ . Neurological convention. The blue cross shows the activation peak.

cortices (see axial MIP slices) in addition to larger cluster extent and a gain in significance level for the stable clusters across the different reconstructors. Similar conclusions can be drawn when looking at Fig. 8[bottom] for  $R = 4$ . Complementary results are available in Table 3 for  $R = 2$  and  $R = 4$  and numerically confirms this visual comparison:

- Whatever the reconstruction method in use, the statistical performance is much more significant using  $R = 2$ , especially at the cluster level since the cluster extent decreases by one order of magnitude.
- Voxel and cluster-level results are enhanced using the 4D-UWR-SENSE approach instead of the mSENSE reconstruction or its early UWR-SENSE version.

Fig. 9 reports similar group-level MIP results for  $R = 2$  and  $R = 4$  concerning the Lc-Rc contrast. It is shown that whatever the acceleration factor  $R$  in use, our pipeline enables to detect a much more spatially extended activation area in the motor cortex. This visual inspection is quantitatively confirmed in Table 4 when comparing the detected clusters using our 4D-UWR-SENSE approach with those found by mSENSE, again irrespective of  $R$ .

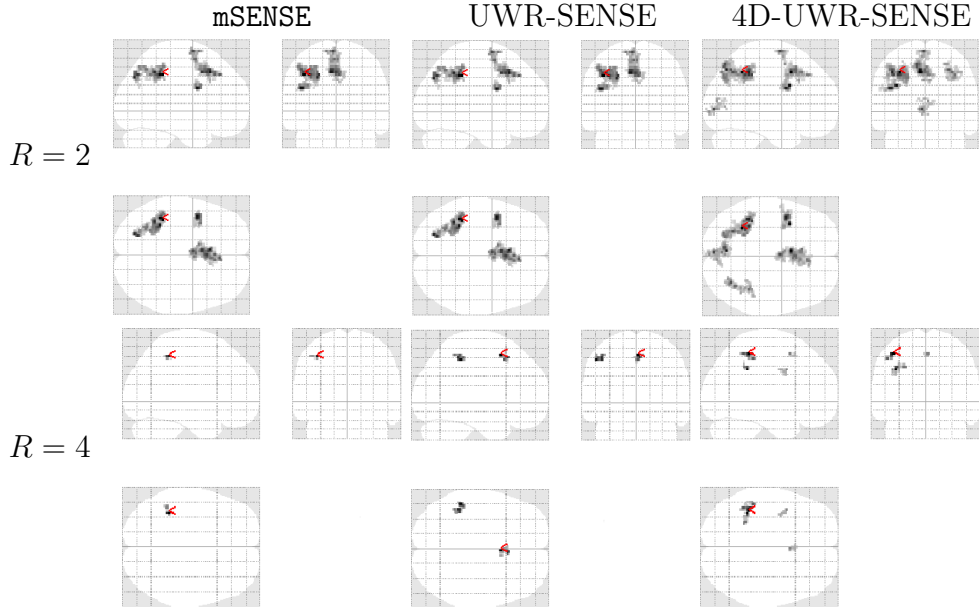


Figure 8: Group-level student- $t$  maps for the aC-aS contrast where data have been reconstructed using the mSENSE, UWR-SENSE and 4D-UWR-SENSE for  $R = 2$  and  $R = 4$ . Neurological convention. Red arrows indicate the global maximum activation peak.

Finally, the 4D-UWR-SENSE algorithm outperforms the UWR-SENSE one, which corroborates the benefits of the proposed spatio-temporal regularization scheme.

## 5. Discussion and conclusion

The contribution of the present paper was twofold. First, we proposed a novel reconstruction method that relies on 3D wavelet transform and accounts for temporal dependencies in successive fMRI volumes. Second, our particular interest was to demonstrate that when artifacts are superimposed to brain activation, this directly impacts subsequent brain activity detection. In this context, we showed that the choice of the parallel imaging reconstruction algorithm impacts the statistical sensitivity in fMRI at the subject and group-levels and may enable whole brain neuroscience studies at high spatial resolution.

Practically speaking, we showed that whole brain acquisition can be routinely used at a spatial in-plane resolution of  $2 \times 2 \text{mm}^2$  in a short and constant

Table 3: Significant statistical results at the group-level for the aC-aS contrast (corrected for multiple comparisons at  $p = 0.05$ ). Images were reconstructed using the mSENSE, UWR-SENSE and 4D-UWR-SENSE algorithms for  $R = 2$  and  $R = 4$ .

|         |              | cluster-level |            | voxel-level |             |             |
|---------|--------------|---------------|------------|-------------|-------------|-------------|
|         |              | p-value       | Size       | p-value     | T-score     | Position    |
| $R = 2$ | mSENSE       | $< 10^{-3}$   | 361        | 0.014       | 7.68        | -6 -22 45   |
|         |              | $< 10^{-3}$   | 331        | 0.014       | 8.23        | -40 -38 42  |
|         |              | $< 10^{-3}$   | 70         | 0.014       | 7.84        | -44 6 27    |
|         | UWR-SENSE    | $< 10^{-3}$   | 361        | 0.014       | 7.68        | -6 22 45    |
|         |              | $< 10^{-3}$   | 331        | 0.014       | 7.68        | -44 -38 42  |
|         |              | $< 10^{-3}$   | 70         | 0.014       | 7.84        | -44 6 27    |
|         | 4D-UWR-SENSE | $< 10^{-3}$   | <b>441</b> | $< 10^{-3}$ | <b>9.45</b> | -32 -50 45  |
|         |              | $< 10^{-3}$   | 338        | $< 10^{-3}$ | 9.37        | -6 12 45    |
|         |              | $< 10^{-3}$   | 152        | 0.010       | 7.19        | 30 -64 48   |
| $R = 4$ | mSENSE       | 0.003         | 14         | 0.737       | 5.13        | -38 -42 51  |
|         | UWR-SENSE    | $< 10^{-3}$   | <b>41</b>  | 0.274       | 5.78        | -50 -38 -48 |
|         |              | $< 10^{-3}$   | 32         | 0.274       | 5.91        | 2 12 54     |
|         | 4D-UWR-SENSE | $< 10^{-3}$   | 37         | 0.268       | <b>6.46</b> | -40 -40 54  |
|         |              | $< 10^{-3}$   | 25         | 0.268       | 6.37        | -38 -42 36  |
|         |              | $< 10^{-3}$   | 18         | 0.273       | 5           | -42 8 36    |

repetition time (TR = 2.4s) provided that a reliable pMRI reconstruction pipeline is chosen. In this paper, we demonstrated that our 4D-UWR-SENSE reconstruction algorithm meets this desired property. To draw this conclusion, our comparison took place at the statistical analysis level and relied on quantitative criteria (voxel- and cluster-level corrected p-values,  $t$ -scores, peak positions) both at the subject and group levels. In particular, we showed that our 4D-UWR-SENSE contribution outperforms both its UWR-SENSE ancestor [7] and the Siemens mSENSE reconstruction in terms of statistical significance and robustness. This emphasized the benefits of combining temporal and 3D regularizations in the wavelet domain. Interestingly, we exhibited a most significant gain in the more degraded situation ( $R = 4$ ) due to the positive impact of regularization. The strength of our conclusions lies in the reasonable size of our datasets since the same cohort participated to parallel imaging acquisitions using two different acceleration factors ( $R = 2$  and  $R = 4$ ).

At this spatio-temporal compromise ( $2 \times 2 \times 3\text{mm}^3$  and TR = 2.4 s),

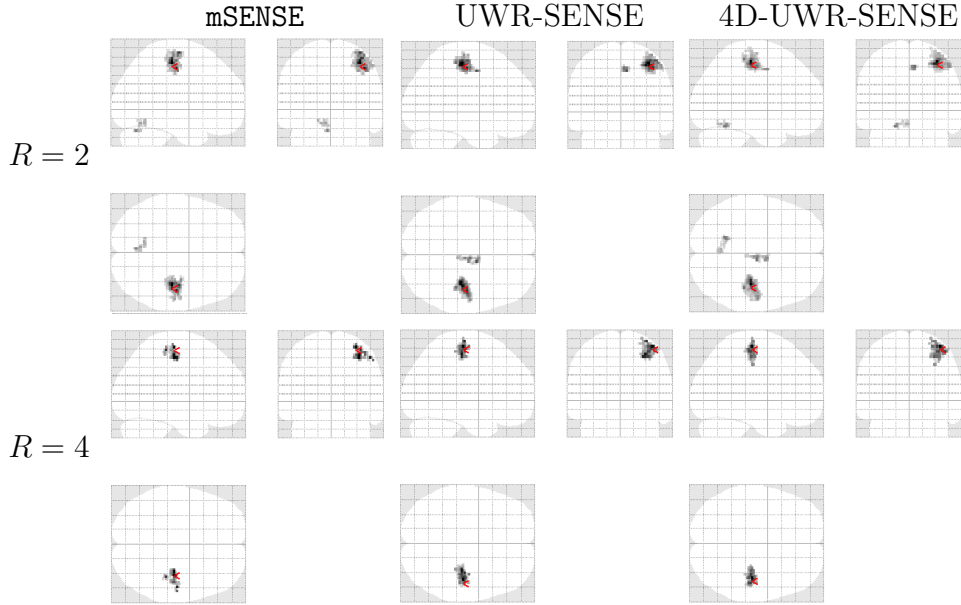


Figure 9: Group-level student- $t$  maps for the Lc-Rc contrast where data have been reconstructed using the mSENSE, UWR-SENSE and 4D-UWR-SENSE for  $R = 2$  and  $R = 4$ . Neurological convention. Red arrows indicate the global maximum activation peak.

Table 4: Significant statistical results at the group-level for the Lc-Rc contrast (corrected for multiple comparisons at  $p = 0.05$ ). Images were reconstructed using the mSENSE, UWR-SENSE and 4D-UWR-SENSE algorithms for  $R = 2$  and  $R = 4$ .

|             |              | cluster-level |             | voxel-level |              |            |
|-------------|--------------|---------------|-------------|-------------|--------------|------------|
|             |              | p-value       | Size        | p-value     | T-score      | Position   |
| $R = 2$     | mSENSE       | $< 10^{-3}$   | 354         | $< 10^{-3}$ | 9.48         | 38 -22 54  |
|             |              | 0.001         | 44          | 0.665       | 6.09         | -4 -68 -24 |
|             | UWR-SENSE    | $< 10^{-3}$   | 350         | 0.005       | 9.83         | 36 -22 57  |
|             |              | $< 10^{-3}$   | 35          | 0.286       | 7.02         | 4 -12 51   |
|             | 4D-UWR-SENSE | $< 10^{-3}$   | <b>377</b>  | 0.001       | <b>11.34</b> | 36 -22 57  |
|             |              | $< 10^{-3}$   | 53          | $< 10^{-3}$ | 7.50         | 8 -14 51   |
| $< 10^{-3}$ |              | 47            | $< 10^{-3}$ | 7.24        | -18 -54 -18  |            |
| $R = 4$     | mSENSE       | $< 10^{-3}$   | 38          | 0.990       | 5.97         | 32 -20 45  |
|             | UWR-SENSE    | $< 10^{-3}$   | 163         | 0.128       | 7.51         | 46 -18 60  |
|             | 4D-UWR-SENSE | $< 10^{-3}$   | <b>180</b>  | 0.111       | <b>7.61</b>  | 46 -18 60  |

we also illustrated the impact of increasing the acceleration factor (passing from  $R = 2$  to  $R = 4$ ) on the statistical sensitivity at the subject and group levels for a given reconstruction algorithm. We performed this comparison to anticipate what could be the statistical performance for detecting evoked brain activity on data requiring this acceleration level, such as high spatial resolution EPI images (eg  $1.5 \times 1.5 \text{mm}^2$  as in-plane resolution) acquired at the same short TR. Our conclusions were balanced depending on the contrast of interest: when looking at the **aC-aS** contrast, which involves in the fronto-parietal circuit, it turned out that  $R = 4$  was not reliable enough to recover group-level significant activity at 3 Tesla: the SNR loss was too important and should be compensated by an increase of the static magnetic field (eg passing from 3 to 7 Tesla). However, the situation is less dramatic or even acceptable for the **Lc-Rc** motor contrast, which elicits activation in motor regions: Our results brought evidence that the 4D-UWR-SENSE approach enabled the use of  $R = 4$  for this contrast.

To summarize, the compromise between the acceleration factor and spatial in-plane resolution should be selected with care depending on the regions involved in the fMRI paradigm. As a consequence, high resolution fMRI studies can be conducted using high speed acquisition (short TR and large  $R$  value) provided that the expected BOLD effect is strong, as experienced in primary motor, visual and auditory cortices. Of course, the use of an optimized reconstruction method such as the one proposed is a pre-requisite to shift this compromise towards larger  $R$  values and higher spatial resolution and could be optimally combined with ultra high magnetic fields.

A direct extension of the present work, which is actually in progress, consists in studying the impact of tight frames instead of wavelet basis to define shift-invariant transformation [7]. However, unsupervised reconstruction becomes more challenging in this framework since the estimation of hyperparameters becomes cumbersome (see [8] for details). Ongoing work will concern the combination of the present contribution with the joint detection estimation approach of evoked activity [27, 42] to go beyond the GLM framework and measure how the pMRI reconstruction algorithm also impacts HRF estimation. Another extension would concern the combination of our wavelet-regularized reconstruction with the WSPM approach [40] in which statistical analysis is directly performed in the wavelet transform domain.

## Appendix A. Maximum likelihood estimation of regularization parameters

A rigorous way of addressing the regularization parameter choice would be to consider that the sum of the regularization functions  $g$  and  $h$  corresponds to the minus-log-likelihood of a prior distribution  $f(\cdot; \Theta)$  where  $\Theta = (\boldsymbol{\mu}_{a,j_{\max}}, \boldsymbol{\alpha}_{a,j_{\max}}, \boldsymbol{\beta}_{a,j_{\max}}, (\boldsymbol{\mu}_{o,j}, \boldsymbol{\alpha}_{o,j}, \boldsymbol{\beta}_{o,j})_{o \in \mathbb{O}, 1 \leq j \leq j_{\max}}, \kappa, p)$ , and to maximize the *integrated* likelihood of the data. This would however entail two main difficulties. On the one hand, this would require to integrate out the sought image decomposition  $\zeta$  and to iterate between image reconstruction and hyper-parameter estimation. Methods allowing us to perform this task are computationally intensive [17]. On the second hand, the partition function of the distribution  $f(\cdot; \Theta)$  does not take a closed form and we would thus need to resort to numerical methods [41, 38, 37] to compute it. To alleviate the computational burden, akin to [19] we shall proceed differently by assuming that a reference full FOV image  $\tilde{\rho}$  is available, and so is its wavelet decomposition  $\tilde{\zeta} = T\tilde{\rho}$ . In practice, our reference image  $\tilde{\rho}$  is obtained using 1D-SENSE reconstruction at the same  $R$  value. We then apply an approximate ML procedure which consists of estimating separately the spatial and temporal parameters. Although this approach is not optimal from a theoretical standpoint, it is quite simple and it was observed to provide satisfactory results in practice. Alternative solutions based on Monte Carlo methods [8] or Stein's principle [10] can also be thought of, at the expense of an additional computational complexity.

### Appendix A.1. Spatial regularization parameters

For the spatial hyper-parameter estimation task, we will assume that the real and imaginary parts of the wavelet coefficients<sup>6</sup> are modelled by the following *Generalized Gauss-Laplace* (GGL) distribution:

$$\forall \xi \in \mathbb{R}, \quad f(\xi; \mu, \alpha, \beta) = \sqrt{\frac{\beta}{2\pi}} \frac{e^{-(\alpha|\xi-\mu| + \frac{\beta}{2}(\xi-\mu)^2 + \frac{\alpha^2}{2\beta})}}{\operatorname{erfc}(\frac{\alpha}{\sqrt{2\beta}})}. \quad (\text{A.1})$$

For each resolution level  $j$  and orientation  $o$ ,  $\hat{\mu}_{o,j}^{\text{Re}}$ ,  $\hat{\alpha}_{o,j}^{\text{Re}}$  and  $\hat{\beta}_{o,j}^{\text{Re}}$  are estimated from  $\tilde{\zeta}_{o,j}$  as follows (we proceed similarly to estimate  $\hat{\mu}_{o,j}^{\text{Im}}$ ,  $\hat{\alpha}_{o,j}^{\text{Im}}$  and  $\hat{\beta}_{o,j}^{\text{Im}}$  by replacing  $\operatorname{Re}(\cdot)$  by  $\operatorname{Im}(\cdot)$ ):

---

<sup>6</sup>A similar approach is adopted for the approximation coefficients.

$$\begin{aligned}
(\widehat{\mu}_{o,j}^{\text{Re}}, \widehat{\alpha}_{o,j}^{\text{Re}}, \widehat{\beta}_{o,j}^{\text{Re}}) &= \arg \max_{(\mu, \alpha, \beta) \in \mathbb{R} \times \mathbb{R}_+ \times \mathbb{R}_+^*} f(\text{Re}(\widetilde{\zeta}_{o,j}); \mu, \alpha, \beta) \\
&= \arg \max_{(\mu, \alpha, \beta) \in \mathbb{R} \times \mathbb{R}_+ \times \mathbb{R}_+^*} \sum_{k=1}^{K_j} \log f(\text{Re}(\widetilde{\zeta}_{o,j,k}); \mu, \alpha, \beta) \\
&= \arg \min_{(\mu, \alpha, \beta) \in \mathbb{R} \times \mathbb{R}_+ \times \mathbb{R}_+^*} \left\{ \alpha \sum_{k=1}^{K_j} |\text{Re}(\widetilde{\zeta}_{o,j,k} - \mu)| + \frac{\beta}{2} \sum_{k=1}^{K_j} |\text{Re}(\widetilde{\zeta}_{o,j,k} - \mu)|^2 \right. \\
&\quad \left. + \frac{K_j \alpha^2}{2\beta} - \frac{K_j}{2} \log \beta + K_j \log(\text{erfc}(\frac{\alpha}{\sqrt{2\beta}})) \right\}. \tag{A.2}
\end{aligned}$$

This three-dimensional minimization problem does not admit a closed form solution. Hence, we can compute the ML estimated parameters using the zero-order Powell optimization method [2].

#### *Appendix A.2. Temporal regularization parameter*

For the temporal hyper-parameter estimation task, we will assume that, at a given voxel, the temporal noise is distributed according to the following generalized Gaussian (GG) distribution:

$$\forall \epsilon \in \mathbb{R}, \quad f(\epsilon; \kappa, p) = \frac{p\kappa^{1/p} e^{-\kappa|\epsilon|^p}}{2\Gamma(1/p)}. \tag{A.3}$$

Akin to the spatial hyper-parameter estimation, reference images  $(\widetilde{\rho}^t)_{1 \leq t \leq N_r}$  are made available based on a 1D-SENSE reconstruction, where  $\forall t \in \{1, \dots, N_r\}$ ,  $\widetilde{\rho}^t = T^* \widetilde{\zeta}^t$ . We consider that at spatial position  $\mathbf{r}$ , the temporal noise vector  $\boldsymbol{\epsilon}_{\mathbf{r}} = [\widetilde{\rho}^2(\mathbf{r}) - \widetilde{\rho}^1(\mathbf{r}), \widetilde{\rho}^3(\mathbf{r}) - \widetilde{\rho}^2(\mathbf{r}), \dots, \widetilde{\rho}^{N_r}(\mathbf{r}) - \widetilde{\rho}^{N_r-1}(\mathbf{r})]^\top$  is a realization of a full independent GG prior distribution and we adjust the temporal hyper-parameter vector  $(\kappa, p)$  directly from it. It should be noted here that the considered model for the temporal noise accounts for correlations between successive observations usually considered in the fMRI literature. It also presents more flexibility than the Gaussian model, which corresponds to the particular case when  $p = 2$ . Estimates  $\widehat{\kappa}$  and  $\widehat{p}$  of the

parameters are then obtained as follows:

$$\begin{aligned}
(\widehat{\kappa}, \widehat{p}) &= \arg \max_{(\kappa, p) \in \mathbb{R}_+ \times [1, +\infty[} f(\boldsymbol{\epsilon}_r; \kappa, p) \\
&= \arg \max_{(\kappa, p) \in \mathbb{R}_+ \times [1, +\infty[} \log f(\boldsymbol{\epsilon}_r; \kappa, p) \\
&= \arg \min_{(\kappa, p) \in \mathbb{R}_+ \times [1, +\infty[} \kappa \sum_{t=1}^{N_r-1} |\widetilde{\rho}^{t+1}(\mathbf{r}) - \widetilde{\rho}^t(\mathbf{r})|^p - (N_r - 1) \log \left( \frac{p\kappa^{1/p}}{2\Gamma(1/p)} \right).
\end{aligned} \tag{A.4}$$

Note that in the above minimization, for a given value of  $p$ , the optimal value of  $\kappa$  admits the following closed form:

$$\widehat{\kappa} = \frac{N_r - 1}{p \sum_{t=1}^{N_r-1} |\widetilde{\rho}^{t+1}(\mathbf{r}) - \widetilde{\rho}^t(\mathbf{r})|^p}. \tag{A.5}$$

A zero-order Powell optimization method can then be used to solve the resulting one-variable minimization problem. To reduce the computational complexity of this estimation, it is only performed on the brain mask, and the temporal regularization parameter  $\kappa$  is set to zero for voxels belonging to the image background.

## Appendix B. Optimization procedure for the 4D reconstruction

We first recall that

$$\mathcal{J}_{\text{ST}}(\zeta) = \mathcal{J}_{\text{TWLS}}(\zeta) + g(\zeta) + h(\zeta) \tag{B.1}$$

where  $\mathcal{J}_{\text{TWLS}}$  is defined as

$$\begin{aligned}
\mathcal{J}_{\text{TWLS}}(\zeta) &= \sum_{t=1}^{N_r} \mathcal{J}_{\text{WLS}}(\zeta^t) \\
&= \sum_{t=1}^{N_r} \sum_{\mathbf{r} \in \{1, \dots, X\} \times \{1, \dots, Y/R\} \times \{1, \dots, Z\}} \|\mathbf{d}^t(\mathbf{r}) - \mathbf{S}(\mathbf{r})(T^* \zeta^t)(\mathbf{r})\|_{\Psi^{-1}}^2.
\end{aligned} \tag{B.2}$$

The minimization of  $\mathcal{J}_{\text{ST}}$  is performed by resorting to the concept of proximity operators [28], which was found to be fruitful in a number of recent works in convex optimization [9, 14, 13]. In what follows, we recall the definition of a proximity operator:

**Definition Appendix B.1** [28] *Let  $\Gamma_0(\chi)$  be the class of lower semicontinuous convex functions from a separable real Hilbert space  $\chi$  to  $] -\infty, +\infty]$  and let  $\varphi \in \Gamma_0(\chi)$ . For every  $\mathbf{x} \in \chi$ , the function  $\varphi + \|\cdot - \mathbf{x}\|^2/2$  achieves its infimum at a unique point denoted by  $\text{prox}_\varphi \mathbf{x}$ . The operator  $\text{prox}_\varphi : \chi \rightarrow \chi$  is the proximity operator of  $\varphi$ .*

In this work, as the observed data are complex-valued, the definition of proximity operators is extended to a class of convex functions defined for complex-valued variables. For the function

$$\begin{aligned} \Phi: \mathbb{C}^K &\rightarrow ] -\infty, +\infty] \\ x &\mapsto \phi^{\text{Re}}(\text{Re}(x)) + \phi^{\text{Im}}(\text{Im}(x)), \end{aligned} \quad (\text{B.3})$$

where  $\phi^{\text{Re}}$  and  $\phi^{\text{Im}}$  are functions in  $\Gamma_0(\mathbb{R}^K)$  and  $\text{Re}(x)$  (resp.  $\text{Im}(x)$ ) is the vector of the real parts (resp. imaginary parts) of the components of  $x \in \mathbb{C}^K$ , the proximity operator is defined as

$$\begin{aligned} \text{prox}_\Phi: \mathbb{C}^K &\rightarrow \mathbb{C}^K \\ x &\mapsto \text{prox}_{\phi^{\text{Re}}}(\text{Re}(x)) + i \text{prox}_{\phi^{\text{Im}}}(\text{Im}(x)). \end{aligned} \quad (\text{B.4})$$

Let us now provide the expression of the proximity operators involved in our reconstruction problem.

#### *Appendix B.1. Proximity operator of the data fidelity term*

According to standard rules on the calculation of proximity operators [13, Table 1.1], the proximity operator of the data fidelity term  $\mathcal{J}_{\text{WLS}}$  is given for every vector of coefficients  $\zeta^t$  (with  $t \in \{1, \dots, N_r\}$ ) by  $\text{prox}_{\mathcal{J}_{\text{WLS}}}(\zeta^t) = T u^t$ , where the image  $u^t$  is such that  $\forall \mathbf{r} \in \{1, \dots, X\} \times \{1, \dots, Y/R\} \times \{1, \dots, Z\}$ ,

$$\mathbf{u}^t(\mathbf{r}) = (\mathbf{I}_R + 2\mathbf{S}^{\text{H}}(\mathbf{r})\mathbf{\Psi}^{-1}\mathbf{S}(\mathbf{r}))^{-1}(\boldsymbol{\rho}^t(\mathbf{r}) + 2\mathbf{S}^{\text{H}}(\mathbf{r})\mathbf{\Psi}^{-1}\mathbf{d}^t(\mathbf{r})), \quad (\text{B.5})$$

where  $\boldsymbol{\rho}^t = T^* \zeta^t$ .

#### *Appendix B.2. Proximity operator of the spatial regularization function*

According to [7], for every resolution level  $j$  and orientation  $o$ , the proximity operator of the spatial regularization function  $\Phi_{o,j}$  is given by

$$\begin{aligned} \forall \xi \in \mathbb{C}, \quad \text{prox}_{\Phi_{o,j}} \xi &= \frac{\text{sign}(\text{Re}(\xi - \mu_{o,j}))}{\beta_{o,j}^{\text{Re}} + 1} \max\{|\text{Re}(\xi - \mu_{o,j})| - \alpha_{o,j}^{\text{Re}}, 0\} \\ &+ i \frac{\text{sign}(\text{Im}(\xi - \mu_{o,j}))}{\beta_{o,j}^{\text{Im}} + 1} \max\{|\text{Im}(\xi - \mu_{o,j})| - \alpha_{o,j}^{\text{Im}}, 0\} + \mu_{o,j} \end{aligned} \quad (\text{B.6})$$

where the sign function is defined as follows:

$$\forall \xi \in \mathbb{R}, \quad \text{sign}(\xi) = \begin{cases} +1 & \text{if } \xi \geq 0 \\ -1 & \text{otherwise.} \end{cases}$$

*Appendix B.3. Proximity operator of the temporal regularization function*

A simple expression of the proximity operator of function  $h$  is not available. We thus propose to split this regularization term as a sum of two more tractable functions  $h_1$  and  $h_2$ :

$$h_1(\zeta) = \kappa \sum_{t=1}^{N_r/2} \|T^* \zeta^{2t} - T^* \zeta^{2t-1}\|_p^p \quad (\text{B.7})$$

and

$$h_2(\zeta) = \kappa \sum_{t=1}^{N_r/2-1} \|T^* \zeta^{2t+1} - T^* \zeta^{2t}\|_p^p. \quad (\text{B.8})$$

Since  $h_1$  (resp.  $h_2$ ) is separable w.r.t the time variable  $t$ , its proximity operator can easily be calculated based on the proximity operator of each of the involved terms in the sum of Eq. (B.7) (resp. Eq. (B.8)).

Indeed, let us consider the following function

$$\begin{aligned} \Psi : \mathbb{C}^K \times \mathbb{C}^K &\longrightarrow \mathbb{R} \\ (\zeta^t, \zeta^{t-1}) &\mapsto \kappa \|T^* \zeta^t - T^* \zeta^{t-1}\|_p^p = \psi \circ H(\zeta^t, \zeta^{t-1}), \end{aligned} \quad (\text{B.9})$$

where  $\psi(\cdot) = \kappa \|T^* \cdot\|_p^p$  and  $H$  is the linear operator defined as

$$\begin{aligned} H : \mathbb{C}^K \times \mathbb{C}^K &\longrightarrow \mathbb{C}^K \\ (a, b) &\mapsto a - b. \end{aligned} \quad (\text{B.10})$$

Its associated adjoint operator  $H^*$  is therefore given by

$$\begin{aligned} H^* : \mathbb{C}^K &\longrightarrow \mathbb{C}^K \times \mathbb{C}^K \\ a &\mapsto (a, -a). \end{aligned} \quad (\text{B.11})$$

Since we have  $HH^* = 2\text{Id}$ , the proximity operator of  $\Psi$  can easily be calculated using [11, Prop. 11]:

$$\text{prox}_\Psi = \text{prox}_{\psi \circ H} = \text{Id} + \frac{1}{2} H^* \circ (\text{prox}_{2\psi} - \text{Id}) \circ H. \quad (\text{B.12})$$

The calculation of  $\text{prox}_{2\psi}$  is discussed in [9].

#### Appendix B.4. Parallel Proximal Algorithm (PPXA)

The function to be minimized has been reexpressed as

$$\begin{aligned} \mathcal{J}_{\text{ST}}(\zeta) = & \sum_{t=1}^{N_r} \sum_{\mathbf{r} \in \{1, \dots, X\} \times \{1, \dots, Y/R\} \times \{1, \dots, Z\}} \|\mathbf{d}^t(\mathbf{r}) - \mathbf{S}(\mathbf{r})(T^* \zeta^t)(\mathbf{r})\|_{\Psi^{-1}}^2 + g(\zeta^t) \\ & + h_1(\zeta^t) + h_2(\zeta^t). \end{aligned} \quad (\text{B.13})$$

Since  $\mathcal{J}_{\text{ST}}$  is made up of more than two non-necessarily differentiable terms, an appropriate solution for minimizing such an optimality criterion is the PPXA [12]. In particular, it is important to note that this algorithm does not require subiterations as was the case for one of the algorithms proposed in [7]. In addition, the computations in this algorithm can be performed in a parallel manner and the convergence of the algorithm to an optimal solution to the minimization problem is guaranteed.

The resulting algorithm for the minimization of the optimality criterion in Eq. (B.13) is given in Algorithm 1. In this algorithm, the weights  $\omega_i$  have been fixed to 1/4 for every  $i \in \{1, \dots, 4\}$ . The parameter  $\gamma$  has been set to 200 since this value seems to give the fastest convergence in practice. The stopping parameter  $\varepsilon$  has been set to  $10^{-4}$ . Using these parameters, the algorithm usually converges in less than 50 iterations.

## References

- [1] Aguirre, G. K., Zarahn, E., D’Esposito, M., Apr. 1997. Empirical analysis of BOLD fMRI statistics. II. Spatially smoothed data collected under null-hypothesis and experimental conditions. *NeuroImage* 5 (3), 199–212.
- [2] Bertsekas, D. P., 1995. *Nonlinear programming*, Second Edition. Athena Scientific, Belmont, USA.
- [3] Boulant, N., Mangin, J.-F., Amadon, A., 2009. Counteracting radio frequency inhomogeneity in the human brain at 7 Tesla using strongly modulating pulses. *Magnetic Resonance in Medicine* 61 (5), 1165–1172.
- [4] Brett, M., Penny, W., Kiebel, S., 2004. Introduction to random field theory. In: Frackowiak, R., Friston, K., Fritch, C., Dolan, R., Price, C., Penny, W. (Eds.), *Human Brain Function*, 2nd Edition. Academic Press, pp. 867–880.
- [5] Chaari, L., Mériaux, S., Pesquet, J.-C., Ciuciu, P., Nov. 7-10 2010. Impact of the parallel imaging reconstruction algorithm on brain activity detection in fMRI. In: 3rd Intern. Symp. on Appl. Sci in Biomed. and Comm. Technol (ISABEL). Rome, Italy, pp. 1–5.

---

**Algorithm 1 4D-UWR-SENSE: spatio-temporal regularized reconstruction.**


---

Set  $(\gamma, \varepsilon) \in ]0, +\infty[^2$ ,  $(\omega_i)_{1 \leq i \leq 4} \in ]0, 1[^4$  such that  $\sum_{i=1}^4 \omega_i = 1$ ,  $(\zeta_i^{(n)})_{1 \leq i \leq 4} \in (\mathbb{C}^{K \times N_r})^4$  where  $\zeta_i^{(n)} = (\zeta_i^{1,(n)}, \zeta_i^{2,(n)}, \dots, \zeta_i^{N_r,(n)})$ ,  $n = 0$ , and  $\zeta_i^{t,(n)} = ((\zeta_{i,a}^{t,(n)}), ((\zeta_{i,o,j}^{t,(n)}))_{o \in \mathbb{O}, 1 \leq j \leq j_{\max}})$  for every  $i \in \{1, \dots, 4\}$  and  $t \in \{1, \dots, N_r\}$ . Set also  $\zeta^{(n)} = \sum_{i=1}^4 \omega_i \zeta_i^{(n)}$  and  $\mathcal{J}^{(n)} = 0$ .

- 1: **repeat**
- 2:   Set  $p_4^{1,(n)} = \zeta_4^{1,(n)}$ .
- 3:   **for**  $t = 1$  to  $N_r$  **do**
- 4:     Compute  $p_1^{t,(n)} = \text{prox}_{\gamma \mathcal{J}_{\text{WLS}}/\omega_1}(\zeta_1^{t,(n)})$ .
- 5:     Compute  $p_2^{t,(n)} = (\text{prox}_{\gamma \Phi_a/\omega_2}(\zeta_{2,a}^{t,(n)}), (\text{prox}_{\gamma \Phi_{o,j}/\omega_2}(\zeta_{2,o,j}^{t,(n)}))_{o \in \mathbb{O}, 1 \leq j \leq j_{\max}})$ .
- 6:     **if**  $t$  is even **then**
- 7:       calculate  $(p_3^{t,(n)}, p_3^{t-1,(n)}) = \text{prox}_{\gamma \Psi/\omega_3}(\zeta_3^{t,(n)}, \zeta_3^{t-1,(n)})$
- 8:     **else if**  $t$  is odd and  $t > 1$  **then**
- 9:       calculate  $(p_4^{t,(n)}, p_4^{t-1,(n)}) = \text{prox}_{\gamma \Psi/\omega_4}(\zeta_4^{t,(n)}, \zeta_4^{t-1,(n)})$ .
- 10:    **end if**
- 11:    **if**  $t > 1$  **then**
- 12:      Set  $P^{t-1,(n)} = \sum_{i=1}^4 \omega_i p_i^{t-1,(n)}$ .
- 13:    **end if**
- 14:    **end for**
- 15:    Set  $p_4^{N_r,(n)} = \zeta_4^{N_r,(n)}$ .
- 16:    Set  $P^{N_r,(n)} = \sum_{i=1}^4 \omega_i p_i^{N_r,(n)}$ .
- 17:    Set  $P^{(n)} = (P^{1,(n)}, P^{2,(n)}, \dots, P^{N_r,(n)})$ .
- 18:    Set  $\lambda_n \in [0, 2]$ .
- 19:    **for**  $i = 1$  to  $4$  **do**
- 20:      Set  $p_i^{(n)} = (p_i^{1,(n)}, p_i^{2,(n)}, \dots, p_i^{N_r,(n)})$ .
- 21:       $\zeta_i^{(n)} = \zeta_i^{(n)} + \lambda_n (2P^{(n)} - \zeta^{(n)} - p_i^{(n)})$ .
- 22:    **end for**
- 23:     $\zeta^{(n+1)} = \zeta^{(n)} + \lambda_n (P^{(n)} - \zeta^{(n)})$ .
- 24:     $n \leftarrow n + 1$ .
- 25: **until**  $|\mathcal{J}_{\text{ST}}(\zeta^{(n)}) - \mathcal{J}_{\text{ST}}(\zeta^{(n-1)})| \leq \varepsilon \mathcal{J}_{\text{ST}}(\zeta^{(n-1)})$ .
- 26: Set  $\hat{\zeta} = \zeta^{(n)}$ .
- 27: **return**  $\hat{\rho}^t = T^* \hat{\zeta}^t$  for every  $t \in \{1, \dots, N_r\}$ .

---

- [6] Chaari, L., Pesquet, J.-C., Benazza-Benyahia, A., Ciuciu, P., May 14-17 2008. Auto-calibrated parallel MRI reconstruction in the wavelet domain. In: *IEEE Int. Symp. on Biomed. Imag. (ISBI)*. Paris, France, pp. 756–759.
- [7] Chaari, L., Pesquet, J.-C., Benazza-Benyahia, A., Ciuciu, P., Nov. 2011. A wavelet-based regularized reconstruction algorithm for SENSE parallel MRI with applications to neuroimaging. *Medical Image Analysis* 15 (2), 185–201.
- [8] Chaari, L., Pesquet, J.-C., Tourneret, J.-Y., Ciuciu, P., Benazza-Benyahia, A., Nov. 2010. A hierarchical Bayesian model for frame representation. *IEEE Trans. on Signal Process.* 58 (11), 5560–5571.
- [9] Chaux, C., Combettes, P., Pesquet, J.-C., Wajs, V., Aug. 2007. A variational formulation for frame-based inverse problems. *Inverse Problems* 23 (4), 1495–1518.
- [10] Chaux, C., Duval, L., Benazza-Benyahia, A., Pesquet, J.-C., Aug. 2008. A nonlinear Stein based estimator for multichannel image denoising. *IEEE Transactions on Signal Processing* 56 (8), 3855–3870.
- [11] Combettes, P. L., Pesquet, J.-C., December 2007. A Douglas-Rachford splitting approach to nonsmooth convex variational signal recovery. *IEEE Journal of Selected Topics in Signal Processing* 1 (4), 564–574.
- [12] Combettes, P. L., Pesquet, J.-C., Dec. 2008. A proximal decomposition method for solving convex variational inverse problems. *Inverse Problems* 24 (6), 27.
- [13] Combettes, P. L., Pesquet, J.-C., 2010. Proximal splitting methods in signal processing. In: Bauschke, H. H., Burachik, R., Combettes, P. L., Elser, V., Luke, D. R., Wolkowicz, H. (Eds.), *Fixed-Point Algorithms for Inverse Problems in Science and Engineering*. Springer Verlag, New York, Ch. 1, pp. 185–212.
- [14] Combettes, P. L., Wajs, V. R., 2005. Signal recovery by proximal forward-backward splitting. *Multiscale Modeling and Simulation* 4, 1168–1200.
- [15] Daubechies, I., 1992. *Ten Lectures on Wavelets*. Society for Industrial and Applied Mathematics, Philadelphia.
- [16] Dehaene, S., 1999. Cerebral bases of number processing and calculation. In: Gazzaniga, M. (Ed.), *The New Cognitive Neurosciences*. MIT Press, Cambridge, Ch. 68, pp. 987–998.
- [17] Dempster, A., Laird, A., Rubin, D., 1977. Maximum likelihood from incomplete data via the EM algorithm (with discussion). *Journal of the Royal Statistical Society, Series B* 39, 1–38.
- [18] Griswold, M. A., Jakob, P. M., Heidemann, R. M., Nittka, M., Jellus, V., Wang, J., Kiefer, B., Haase, A., Jun. 2002. Generalized autocalibrating partially parallel acquisitions GRAPPA. *Magnetic Resonance in Medicine* 47 (6), 1202–1210.

- [19] Jalobeanu, A., Blanc-Féraud, L., Zerubia, J., Feb. 2002. Hyperparameter estimation for satellite image restoration using a MCMC maximum likelihood method. *Pattern Recognition* 35 (2).
- [20] Katscher, U., Börnert, P., Leussler, C., van den Brink, J. S., Jul. 2003. Transmit SENSE. *Magnetic Resonance in Medicine* 49 (1), 144–150.
- [21] Keeling, S. L., Jul. 2003. Total variation based convex filters for medical imaging. *Applied Mathematics and Computation* 139 (1), 101–119.
- [22] Kochunov, P., Rivière, D., Lancaster, J., Mangin, J.-F., Cointepas, Y., Glahn, D., Fox, P., Rogers, J., 2005. Development of high-resolution MRI imaging and image processing for live and post-mortem primates. In: *In Proc. 11th HBM CD-Rom*. Vol. 26 (1). Toronto, Canada.
- [23] Liang, Z. P., Bammer, R., Ji, J., Pelc, N. J., Glover, G. H., May 18-24 2002. Making better SENSE: wavelet denoising, Tikhonov regularization, and total least squares. In: *International Society for Magnetic Resonance in Medicine*. Hawaiï, USA, p. 2388.
- [24] Liu, B., Abdelsalam, E., Sheng, J., , Ying, L., May 14-17 2008. Improved spiral SENSE reconstruction using a multiscale wavelet model. In: *IEEE Int. Symp. on Biomed. Imag. Paris, France*, pp. 1505–1508.
- [25] Liu, B., King, K., Steckner, M., Xie, J., Sheng, J., Ying, L., Dec. 2008. Regularized sensitivity encoding (SENSE) reconstruction using Bregman iterations. *Magnetic Resonance in Medicine* 61 (1), 145 – 152.
- [26] M. Lustig, D. D., Pauly, J. M., 2007. Sparse MRI: The application of compressed sensing for rapid mr imaging. *Magnetic Resonance in Medicine* 58, 1182–1195.
- [27] Makni, S., Idier, J., Vincent, T., Thirion, B., Dehaene-Lambertz, G., Ciuciu, P., Jul. 2008. A fully Bayesian approach to the parcel-based detection-estimation of brain activity in fMRI. *Neuroimage* 41 (3), 941–969.
- [28] Moreau, J.-J., 1965. Proximité et dualité dans un espace hilbertien. *Bulletin de la Société Mathématique de France* 93, 273–299.
- [29] Nichols, T., Hayasaka, S., 2003. Controlling the Familywise Error Rate in Functional Neuroimaging: A Comparative Review. *Statistical Methods in Medical Research* 12 (5), 419–446.
- [30] Penny, W., Flandin, G., Trujillo-Bareto, N., 2007. Bayesian Comparison of Spatially Regularised General Linear Models. *Human Brain Mapping* 28 (4), 275–293.
- [31] Penny, W. D., Kiebel, S., Friston, K. J., Jul. 2003. Variational Bayesian inference for fMRI time series. *Neuroimage* 19 (3), 727–741.

- [32] Pinel, P., Thirion, B., Mériaux, S., Jobert, A., Serres, J., Le Bihan, D., Poline, J.-B., Dehaene, S., Oct. 2007. Fast reproducible identification and large-scale databasing of individual functional cognitive networks. *BMC Neurosci.* 8 (1), 91.
- [33] Pruessmann, K. P., Weiger, M., Scheidegger, M. B., Boesiger, P., Jul. 1999. SENSE : sensitivity encoding for fast MRI. *Magnetic Resonance in Medicine* 42 (5), 952–962.
- [34] Pruessmann, K. P., Weiger, M., Scheidegger, M. B., Boesiger, P., Jul. 1999. SENSE: sensitivity encoding for fast MRI. *Magnetic Resonance in Medicine* 42 (5), 952–962.
- [35] Purdon, P. L., Weisskoff, R. M., 1998. Effect of temporal autocorrelation due to physiological noise and stimulus paradigm on voxel-level false-positive rates in fMRI. *Human Brain Mapping* 6 (4), 239–249.
- [36] Rabrait, C., Ciuciu, P., Ribès, A., Poupon, C., Leroux, P., Lebon, V., Dehaene-Lambertz, G., Bihan, D. L., Lethimonnier, F., Mar. 2008. High temporal resolution functional MRI using parallel echo volume imaging. *Magnetic Resonance Imaging* 27 (4), 744–753.
- [37] Risser, L., Idier, J., Ciuciu, P., Nov. 2009. Bilinear extrapolation scheme for fast estimation of 3D Ising field partition function. Application to fMRI time course analysis. In: 16th Proc. IEEE ICIP. Cairo, Egypt, pp. 833–836.
- [38] Risser, L., Vincent, T., Ciuciu, P., Idier, J., Sep. 2009. Robust extrapolation scheme for fast estimation of 3D Ising field partition functions. application to within-subject fMRI data analysis. In: 12th Proc. Medical Image Computing and Computer Assisted Intervention. Springer Verlag Berlin Heidelberg, London, UK, pp. 975–983.
- [39] Sümbül, U., Santos, J. M., Pauly, J. M., Jul. 2009. Improved time series reconstruction for dynamic magnetic resonance imaging. *IEEE Transactions on Medical Imaging* 28 (7), 1093–1104.
- [40] Van De Ville, D., Seghier, M., Lazeyras, F., Blu, T., Unser, M., Oct. 2007. WSPM: Wavelet-based statistical parametric mapping. *Neuroimage* 37 (4), 1205–1217.
- [41] Vieth, M., Kolinski, A., Skolnick, J., Apr. 1995. A simple technique to estimate partition functions and equilibrium constants from Monte Carlo simulations. *Journal of Chemical Physics* 102, 6189–6193.
- [42] Vincent, T., Risser, L., Ciuciu, P., Apr. 2010. Spatially adaptive mixture modeling for analysis of within-subject fMRI time series. *IEEE Transactions on Medical Imaging* 29 (4), 1059–1074.
- [43] Woolrich, M., Jenkinson, M., Brady, J., Smith, S., Feb. 2004. Fully Bayesian spatio-temporal modelling of fMRI data. *IEEE Transactions on Medical Imaging* 23 (2), 213–231.

- [44] Woolrich, M., Ripley, B., Brady, M., Smith, S., Dec. 2001. Temporal autocorrelation in univariate linear modelling of fMRI data. *NeuroImage* 14 (6), 1370–1386.
- [45] Worsley, K., Liao, C., Aston, J., Petre, V., Duncan, G., Morales, F., Evans, A., Jan. 2002. A general statistical analysis for fMRI data. *NeuroImage* 15 (1), 1–15.
- [46] Ying, L., Xu, D., Liang, Z.-P., Sept. 1-5 2004. On Tikhonov regularization for image reconstruction in parallel MRI. In: *IEEE Engineering in Medicine and Biology Society*. San Francisco, USA, pp. 1056–1059.
- [47] Zarahn, E., Aguirre, G. K., D’Esposito, M., Apr. 1997. Empirical analysis of BOLD fMRI statistics. I. Spatially unsmoothed data collected under null-hypothesis conditions. *NeuroImage* 5 (3), 179–197.
- [48] Zou, Y. M., Ying, L., Liu, B., May 30-31 2008. SparseSENSE: application of compressed sensing in parallel MRI. In: *IEEE International Conference on Technology and Applications in Biomedicine*. Shenzhen, China, pp. 127–130.